Unsymmetrical stacking sequences as a novel approach to tailor damage resistance under out-of-plane impact loading

A. Sasikumar*, J. Costa*, D. Trias[1], E.V. González, S.M. García-Rodríguez, P. Maimí

AMADE, Polytechnic School, Universitat de Girona, Campus Montilivi s/n, 17073 Girona, Spain

Abstract

In current composite design, stacking sequence symmetry around the laminate mid-plane is an unarguable constraint to avoid warpage during manufacturing. However, several load cases induce unevenly distributed stresses through the laminate thickness, such that symmetric laminates may not be the optimal solution. In this paper, we explore the damage resistance to out-of-plane low velocity impact loading of an unsymmetrical laminate with zero extension-bending coupling matrix ([B]), thereby assuring no undesired coupling deformations during mechanical or thermal loads. Using impact and quasi-static indentation tests, C-scan inspection and numerical modelling, we compare the damage pattern between an unsymmetrical laminate with ply clustering at the impacted face and a laminate with ply clustering at the non-impacted face (produced by flipping the former laminate upside down). The laminate with clusters at the impacted side exhibits better damage resistance for lower impact energies. More importantly, the location of the damage events obeys the predictions assumed when the laminate was designed, demonstrating the room for improvement by tailoring unsymmetrical laminates to particular load cases.

Keywords: B. Impact behaviour, B. Delamination, C. Damage mechanics, C. Finite element analysis (FEA), Unsymmetrical laminates

---

☆

*Corresponding author : Aravind Sasikumar, Josep Costa

Email addresses: `aravind.sasikumar@udg.edu` (A. Sasikumar), `josep.costa@udg.edu` (J. Costa)

[1]Serra Hunter Fellow.

1. Introduction

Impact loading and the threat it poses to composite structures is a matter of concern for aircraft engineers and researchers. The severity of the impact induced damage and its propagation during in-flight loads is the key research question to be answered as impact damage can reduce the residual strength of a structure by up to 60% [1]. In an effort to improve damage resistance, researchers have gone one step further in laminate design and have proposed non-conventional laminates using dispersed angles [2–4], varying mismatch angle at interfaces [4; 5] or selective ply clustering [6]. Despite the novelty in laminate designing, symmetry around the mid plane of the laminate remains an unquestioned constraint, mainly to avoid warpage during manufacturing and coupling responses under loading [7].

Impact loading is a complex loading case because of the interaction of different damage mechanisms, mainly in terms of matrix cracks and delamination, followed by fibre failure at higher impact energies. The damage scenario is unsymmetrical in the through-the-thickness direction [8; 9]: high contact compressive stresses cause matrix cracks by shear at the vicinity of the impactor (impacted face of the laminate), whereas tensile stresses cause transverse matrix cracking at the non-impacted face of the laminate. These cracks grow into the interfaces and initiate delamination oriented in the direction of the lower plies [8]. Acknowledging that the impacted and non-impacted laminate sides experience different damage mechanisms during impact, the constraint of laminate symmetry needs to be challenged.

Recently, quasi-static indentation (QSI) tests are considered as an alternative to the low velocity impact tests, due to the similarity in the loading responses and the damage characteristics [10–12]. In LVI loading, the impact contact time is long enough to allow the impact waves to get reflected multiple times from the specimen boundaries and hence the resulting impact response is considered purely static loading [13–15].

In this paper, we propose an unsymmetrical laminate with ply clustering at the impacted face of the laminate. As reported in [13], a clustered ply block induces high interlaminar shear stresses thereby triggering delamination at the corresponding ply interface. Here we attempt to use localized ply clusters in the laminate to foster delamination at pre-determined regions. Thanks to the unsymmetrical design, the same laminate, when flipped upside down, produces another stacking sequence with ply clustering at the non-impacted face. Low velocity impact (LVI) and quasi-static indentation responses of these two unsymmetrical laminates are studied in order to shed light on how the initiation and propagation of the delaminations differ when imposed at different locations. Further, numerical results from an in-house finite element model featuring inter and intralaminar damage are compared with the experimental results, followed by an in-depth energy dissipation analysis for each ply and interface of both laminates. To the authors' knowledge, this is the first report on an experimental impact study on an unsymmetrical laminate.

2. Unsymmetrical laminate design

The unsymmetrical laminate was obtained by means of an optimization algorithm (genetic algorithm embedded in the MATLAB optimization toolbox [16]). The objective function was a minimum summation of the terms of the B matrix, with the intention of finding solutions with a null B matrix. A null B matrix assures that there is no extension-bending coupling response [17; 18] and as a result there will be no undesired deformation couplings such as warpage during manufacturing.

In addition to the objective function, the following constraints were also imposed: i) the laminate had to be in-plane quasi-isotropic and balanced with 24 plies; ii) as ply clustering induces delamination at the interfaces of the blocked plies [13; 19], four clusters (one cluster for each orientation, $0°$, $\pm 45°$ and $90°$) were imposed at the impacted side of the unsymmetrical laminate to trigger delamination at these locations; it was also made sure that not more than three plies of the same orientation were stacked together; iii) the surface ply was fixed to be either $45°$ or $-45°$ in order to tackle the shear loads [2]; and iv) a constant mismatch angle of $45°$ was used at the interfaces, thereby avoiding the effect of varied mismatch angled interfaces [4; 5].

The solution, with a zero B matrix was: [-45_2/90_2/45_2/0_3/45/90/-45/0/45/90/-45/0/45/90/-45/0/45/90/-45/0/45/90/-45].

3. Methodology

3.1. Experimental

The unsymmetrical panel was manufactured using Hexcel® IM7/8552 uni-directional prepreg tapes and was cured in an autoclave. Despite being unsymmetrical, the panel had zero warpage after curing; as expected from the design study of the stacking sequence.

Impact specimens of standard 150 x 100 mm dimensions were cut out of the panel with 0° plies aligned in the longer direction. The 24-ply laminate had a cured thickness of 4.36 mm and a ply thickness of 0.182 mm. The specimens cut out were flipped upside down in order to obtain specimens with the same ply clustering at the non-impacted side. The laminate with ply clustering at the impacted side is hereafter called LPCI, and the laminate with ply clustering at the non-impacted side as LPCN (Fig. 1). It is to be noted that flipping a laminate upside down only interchanges the $-45°$ plies with 45° plies, thus both laminates have the same in-plane stiffness in all directions and the same bending stiffnesses in the 0° and 90° directions.

As in [13; 20], impact tests were performed on 150 x 100 mm specimens in accordance with the ASTM D7136/D7136M-15 standards [21] using a CEAST Fractovis Plus instrumented drop-weight tower. The impactor featured a 16 mm in diameter hemispherical tip and the impactor mass was adjusted to 5 kg for the entire study. As the study aims to analyse the low velocity impact response (energy levels that create lesser damage than the barely visible impact damage (BVID) threshold) of the laminates, two LVI energies, 12 J and 18 J, were explored.

QSI tests were performed using an MTS INSIGHT® 50 testing machine with a 50 kN load cell, replicating the same boundary conditions as the impact test. Specimens were placed on a base support with an open window of 125 x 75 mm and clamped at the edges using four rubber pads. Displacement controlled indentation was performed on the specimens at a rate of 1 mm/min using the same indenter configuration as for impact loading. Further details of the test setup are provided in [22].

QSI loading was interrupted for C-scan damage inspection followed by further indentation to the next indenter displacement level, thereby the same specimen was subjected to more than one indentation. A total of 8 indenter displacements (from d= 1.17 mm to 5.4 mm) were investigated, thus obtaining the complete damage evolution starting from the initiation of matrix cracks to complete delamination propagation. The indenter displacements were defined on the go: the indentation was stopped when a load drop or a change in stiffness of the force-displacement response, or an acoustic emission, was noticed.

Pulse-echo mode ultrasonic C-scan inspection was performed on all the QSI specimens after each displacement level and on all the impacted specimens using an OLYMPUS OMNI MX system employing a 5 MHz piezoelectric probe. As C-scan inspection has the drawback of larger delaminations masking the underlying ones, C-scan was performed from both sides of the specimens, and the results presented are the inspections providing the most information.

3.2. Numerical modelling

User-defined constitutive models from Maimí et al. [23; 24] were used to simulate the onset and propagation of intralaminar damage. Apart from the main highlights such as crack closure effects, incorporating in-situ effects [25; 26], and the inclusion of crack band model formulation, the complete description can be found in [27]. The model was implemented as an Abaqus/Explicit VUMAT user-written sub-routine. The interlaminar damage was modelled using the ABAQUS Explicit in-built surface based cohesive behaviour [28], where a contact based interaction is used to model the traction between the contact surfaces to simulate delamination. The delamination initiation is governed by a quadratic stress-based criterion implemented in ABAQUS, whereas delamination evolution is characterised by the mixed mode energy-based propagation criteria proposed by Benzeggagh and Kenane [29]. Formulations of the initiation and propagation criteria are not detailed here but can be found in the work of Tan et al. [30].

This study follows a novel FE modelling approach from González et al. [27]. Interested readers are referred to their work for a more detailed description. Each ply is modelled using a conventional shell element which is sandwiched by surface elements on the top and bottom faces of the ply. The surface elements are tied to the shell elements with rigid tie connectors, thereby transferring the kinematics from the shells to the surface elements. Delamination between two plies is modelled by assigning cohesive surface-based interaction between the bottom face of the surface elements of the top ply and the top face of the surface elements of the bottom ply, as seen in Fig. 2 for an illustrative two plies model.

Clustered plies were modelled as a single shell element layer, leading to a model consisting of 19 layers. S4R conventional shell elements were used for the plies and SFM3D4R for the surface elements. The mesh was finer under the impactor (a refined window of 75 by 75 mm, referenced from the impact centre, with element size, l = 0.5 mm) than elsewhere (l = 4 mm). Moreover, the in-situ effect is accounted for by considering the ply thickness and the ply type (outer and embedded). To avoid excessive element distortion, an element was deleted when the fibre damage variable (d_1) reached 1, whereas the transverse (d_2) and shear damage (d_6) variables were assigned a maximum value of 0.99, and no element deletion was considered. A friction coefficient of μ=0.3 was assumed at the ply interfaces, as this property is not experimentally available. Further details about modelling (impactor, rubber clamps, base plate), contact algorithms, cohesive law shapes are explained in detail in [27; 31; 32]. The material data for IM7/8552 was obtained from [33].

4. Results

4.1. Experimental

The delamination threshold load, F_d, marked by the first clear load drop in the impact curves at 12 J and 18J (Fig. 3), is 30% higher for LPCI than LPCN, thereby

LPCI clearly delays delamination onset compared to LPCN. After the delamination threshold load, a comparatively unstable response associated with intermittent load drops is seen with LPCI over LPCN. Maximum peak load, F_{max}, is approximately the same for both laminates at 12 J, whereas an increase of 12% is observed for LPCN over LPCI at 18 J. The energy dissipation of LPCI is 9% and 22% larger than LPCN for 12 J and 18 J, respectively. A compact quantitative overview of the various damage resistance parameters for both laminates and both impact energies is presented using a radar plot in Fig. 4.

Fig. 5 identifies the delaminated interfaces as well as the dominant delaminations for both laminates. Dominant delaminations are those which govern the total delamination profile, thereby playing a major role in the damage tolerance of the structure [22; 34]. For LPCN, they appeared at all the interfaces within the clustered block (interfaces 15, 16, 17 and 18) and scaled up when moving from 12 J to 18 J. For LPCI, an unsymmetric delamination profile is observed for 12 J, with the dominant delaminations at interfaces within the clustered block at the impacted side (int. 3, 4) as well as just below the clustered block (int. 5, 6, 7). Moving on to the 18 J impact, a rapid growth in the projected delamination size is observed where the dominant delaminations are found outside the cluster block (int. 5, 6, 7), with the 90° oriented delamination (int. 5) almost reaching the impact window boundaries. When both laminates were compared, LPCI displayed a 20% reduced projected delamination area over LPCN for 12 J, whereas at 18 J it was 50% larger.

Unlike the impact tests, QSI tests interrupted for damage inspection provide information about the whole damage process. Fig. 6 shows the load displacement response of a pristine specimen up to the highest indenter displacement (d=5.4 mm) as well as the other indenter displacements (d_i), and the associated applied energies (E_a). The early delamination initiation of LPCN found in the impact test, is observed in the QSI results as well. After the delamination drop, the load deflection response for both LPCN and LPCI from indenter displacement d_3 to d_5 is similar. Beyond this, d_7 to d_8, LPCI shows a relative reduction in the stiffness followed by an increase.

Fig. 7(a) details the complete QSI delamination sequence obtained for both laminates using interrupted C-scan inspections, thus helping to relate each load drop or stiffness change (Fig. 6) to the corresponding delamination or its propagation. C-scan images of displacement d_1 (just after the first load drop of LPCN and before the load drop of LPCI) evidence the presence of delamination (initiated in the clustered block at the non-impacted side) in LPCN and yet there is no delamination initiation in LPCI. The first load drop is related to a simultaneous occurrence of matrix cracks and delamination initiation [9; 14]. Displacement d_2 (immediately after the load drop of LPCI) shows delamination initiation in the clustered block at the impacted side of LPCI and delamination extension at the interfaces of the non-impacted side for LPCN.

Through displacements d_3 to d_5, already formed delaminations propagate in both laminates. The LPCI laminate exhibits dominant delamination mainly at the impacted side, whereas in LPCN delaminations at the interfaces of the non-impacted side dominate. The change in stiffness for LPCI (displacement d_6 in Fig. 6) corresponds to a rapid and unsymmetric growth of delaminations for LPCI within the interfaces 5, 6, 7 at the impacted side). At displacement d_7 (associated with the stiffness increase with LPCI), LPCI has its dominant delamination at interface 5 (oriented in $90°$) develop into the supported region of the clamping (as seen with 18 J impact results), leading to stress redistribution and thereby an increase in stiffness, while LPCN showed further delamination extension. Ultimately, the last displacement resulted in further scaling up of delamination with LPCN, and delamination growing to the specimen edges for LPCI.

Fig. 7(b) depicts a quantitative evolution of the damage resistance parameters for all the indenter displacements. LPCI was seen to be more damage resistant than LPCN, in terms of projected damage area and dent depth, until the displacement of d_6, at which an overturn in the trend is noted. Comparing the impact results of 12 J with the QSI results for the same applied energy (corresponding to d_5), a good correlation is observed with the maximum peak force and the projected delamination area. Moving to 18 J, the QSI results (corresponding to d_7) slightly over-predict the above two parameters compared to the impact results (by 8% and 15%, respectively).

4.2. Numerical

The numerical predictions of the impact response curves, namely the force-deflection and energy evolution curves (Fig. 8), are in excellent agreement with the experimental results, especially with the energy evolution for both laminates at both impact energies. Fig. 8 also depicts the impactor displacements chosen for the numerical analysis of the energy dissipated through intralaminar and interlaminar damage: marked by circles (A to E) for the force response and by dashed lines for the energy-time curves. This figure also distinguishes the energy dissipated through inter and intralaminar damage.

Moving away from the normal convention of comparing only the projected delamination contour or the area, we present a 'virtual C-scan', where along with the delamination profile and area, each delaminated interface is identified and presented as in a C-scan. Fig 9 shows the good agreement between the virtual and experimental C-scan, highlighting the potential of the numerical tools used. With LPCN laminates, the dominating delaminations and their extension is almost replicated in the prediction, although the projected damage area is slightly under-predicted by an average of 8%. For LPCI, dominant delaminated interfaces are correctly predicted, while the unsymmetric delamination extension for 12 J and the rapid growth of the close-to-mid-plane delaminations for 18 J are not, thus the projected damage area is underpredicted.

Fig. 10 illustrates the two laminates along with the amount of energy dissipated for each ply and each interface for both laminates. The figure quantitatively compares the inter- (delamination) and intra- (matrix cracks and fibre failure) laminar energy dissipated for all the plies and interfaces between LPCN and LPCI for 12 J. Note that the different colour codes in the figure represent the energy dissipated within the different displacement steps (A to E, as shown in Fig. 8) considered in the study. The figure also compares (at the bottom) the total energy dissipated (inter- and intralaminar) by the two laminates within the selected displacement steps.

With LPCN, as demonstrated by the experiment, the last four interfaces (15, 16, 17 and 18) dissipate the larger amount of energy through delaminations, whereas with LPCI the interfaces 3, 4 (within the cluster), 5, 6, and 14 dominate. The total energy dissipated by the dominant delaminations of LPCN over its other delaminated interfaces is much higher (int. 15, 16, 17 and 18 account for 30% of the total interlaminar energy dissipated) than for LPCI. In the case of intralaminar damage, the first four plies of both laminates dissipated most of the energy, with LPCI being comparatively higher than LPCN, due to the clustered plies.

Displacement level A (chosen to be before the load drop for LPCN and before the stiffness change for LPCI in the numerical curve, as in Fig. 8) reveals no delamination for both laminates. Most of the delamination energy dissipation is observed at the final loading part, between the points C and D. The same occurs with the intralaminar damage, with local fibre failure being seen at the top two plies in the vicinity of the impactor. Fig. 10 compares the energy dissipation at the laminate level: the average energy dissipated through delaminations is approximately five times higher than that of the intralaminar damage, signifying the dominance of energy disspation through delamination within the energy levels explored. Comparing LPCI and LPCN for 12 J, LPCI dissipates 18% more energy through intralaminar damage, and 17% less through interlaminar damage.

5. Discussion

The experimental results revealed the different damage onset and evolution of the two laminates analysed. Delamination initiates earlier in the laminate with clustered plies at the non-impacted side (LPCN), which is related to the transverse cracks in the plies (at non-impacted side) induced by in-plane tensile loads from laminate bending. These cracks grow into the next available interface to initiate delamination. Clustered plies introduce high bending stiffness mismatch [19], leading to high interlaminar shear stresses at the adjacent interfaces. This triggers delamination and makes clustered plies a weak zone for delamination onset. Additionally, the reduced in-situ effect of the clustered plies favours transverse cracking when compared to the non-clustered plies

[33]. When the transverse crack reaches the adjacent interface, the large energy release rate available acts as a catalyst for delamination. Substantial difference in damage mechanisms was observed when the clustered plies are on the impacted side (LPCI). Impact loading introduces high local out-of-plane compressive stresses at the vicinity of the impactor, which counteract the interlaminar shear stresses and lead to increased interlaminar friction [35]. This can be indirectly ascribed to the increase in mode II fracture toughness at regions close to the impactor, as reported in [36; 37]. This constrains the delamination propagation, as observed in the first two interfaces within the clustered block of LPCI (see Fig. 5).

We also observed that the position of the larger delaminations varies from one laminate to the other. The idea of imposing delaminations at the non-impacted side in LPCN by tailoring clustered plies has paid off, with the dominant delaminations appearing at the interfaces within the clustered block (int. 15, 16, 17 and 18 in Fig. 5). In the case of LPCI, with the suppressed delaminations at the interfaces of the impacted side, the dominant delaminations were seen outside the cluster, due to the high interlaminar shear stresses at the laminate mid-plane. These high stresses trigger transverse shear cracks in the 45° and -45° plies (associated with the interfaces 5, 6 and 7 in Fig. 5) promoting delamination oriented in the 90° ply (which is placed in between the 45° and -45° plies as in Fig. 1). Finally, in terms of impact resistance, LPCI performed better at 12 J impact and earlier stages of indenter displacements (up to d_6). At higher energy levels, the rapid growth of close to mid-plane delaminations induced more damage than in LPCN.

The numerical study identified the local fibre failure caused by the impactor as the prime reason for the high intralaminar energy dissipation at the top plies (at impacted side) for both laminates. Owing to the cluster effect, LPCI showed higher values of intralaminar energy dissipation over LPCN for the top plies. While the same clustered plies of LPCN dissipated most of the energy through interlaminar damage, LPCI clustered plies dissipated it through intralaminar damage. This difference in behaviour signifies how the location in the laminate varies the damage mode and its evolution.

The lack of accuracy of the numerical prediction of LPCI (as in Fig. 8 and Fig. 9), may be attributed to the inability of shell elements to capture the shear matrix cracks from the out-of-plane shear stresses close to the impactor. This could be tackled by incorporating a full three dimensional constitutive behaviour with solid elements [38] followed by a oriented mesh strategy (as demonstrated in [39]), but at the price of a higher computational time.

What is clear from the study, is that damage can be forced to occur at predetermined locations through judicious laminate designing, and thereby tailor the damage resistance. Unsymmetrical stacking designs can facilitate this task and raise the prospect of an improved impact damage resistance. Current numerical tools provide a detailed physical representation of the damage mechanisms, so they can efficiently support this innovative design task. A continuation of this work will be to compare unsymmetrical laminates with symmetric quasi-isotropic laminates in terms of impact damage resistance and tolerance (Compression After Impact) to better assess the prospects of unsymmetrical laminates.

6. Conclusion

For the first time, unsymmetrical stacking sequences have been explored in an experimental low velocity impact framework. We designed an unsymmetrical laminate (with zero extension-bending coupling, and therefore warp-free) with tailored ply clustering at the impacted side, and flipped it upside down to yield a laminate with ply clustering at the non-impacted side. Both these laminates were tested under low velocity impact and quasi-static indentation loading to study their out-of-plane damage resistance. The experimental and numerical results revealed that clustering at the impacted side delayed the threshold load for delamination by 30% and reduced the projected delamination area by 20% for low impact energies. This improvement derived from a higher energy dissipation through intralaminar damage instead of delamination, the most important damage mechanism for the laminate with clusters at the non-impacted side. Damage patterns from both laminates were compared and, importantly, the dominant delaminations were observed at the locations predicted during the laminate design. This paper highlights the opportunity to move away from conventional symmetrical laminate design, thereby giving laminate designers the freedom to tailor the stacking sequence according to the expected stress states of given load cases.

Acknowledgements

The first author would like to thank the Generalitat de Catalunya for the FI-DGR pre-doctoral grant (2017 FI-B1 00089). The authors would like to thank the *Spanish Ministerio de Economía y Competitividad* for the grant coded MAT2015-69491-C3-1-R and supported by FEDER/EU. The authors would also like to thank Airborne Composites SL, Girona, for manufacturing the specimens used in the study.

References

[1] S. Sánchez-Sáez, E. Barbero, R. Zaera, C. Navarro, Compression after impact of thin composite laminates, Composites Science and Technology 65 (13) (2005) 1911–1919.

[2] C. Lopes, O. Seresta, Y. Coquet, Z. Gürdal, P. Camanho, B. Thuis, Low-velocity impact damage on dispersed stacking sequence laminates. Part I: Experiments, Composites Science and Technology 69 (7) (2009) 926–936.

[3] C. Lopes, P. Camanho, Z. Gürdal, P. Maimí, E. González, Low-velocity impact damage on dispersed stacking sequence laminates. Part II: Numerical simulations, Composites Science and Technology 69 (7-8) (2009) 937–947.

[4] Y. Liv, G. Guillamet, J. Costa, E. González, L. Marín, J. Mayugo, Experimental study into compression after impact strength of laminates with conventional and nonconventional ply orientations, Composites Part B: Engineering 126 (7) (2017) 133–142.

[5] T. Sebaey, E. González, C. Lopes, N. Blanco, P. Maimí, J. Costa, Damage resistance and damage tolerance of dispersed CFRP laminates: Effect of the mismatch angle between plies, Composite Structures 101 (2013) 255–264.

[6] T. Sebaey, E. González, C. Lopes, N. Blanco, J. Costa, Damage resistance and damage tolerance of dispersed CFRP laminates: Effect of ply clustering, Composite Structures 106 (2013) 96–103.

[7] C. T. Herakovich, Mechanics of fibrous composites, 1998.

[8] S. Abrate, Impact on Composite Structures, Cambridge University Press, 2005.

[9] A. Wagih, P. Maimí, N. Blanco, J. Costa, A quasi-static indentation test to elucidate the sequence of damage events in low velocity impacts on composite laminates, Composites Part A: Applied Science and Manufacturing 82 (2016) 180–189.

[10] P. A. Lagace, J. E. Williamson, P. Wilson Tsang, E. Wolf, S. Thomas, A preliminary proposition for a test method to measure (impact) damage resistance, Journal of Reinforced Plastics and Composites 12 (5) (1993) 584–601.

[11] S. R. Swanson, Limits of quasi-static solutions in impact of composite structures, Composites Engineering 2 (4) (1992) 261–267.

[12] H. Kaczmarek, S. Maison, Comparative ultrasonic analysis of damage in cfrp under static indentation and low-velocity impact, Composites science and technology 51 (1) (1994) 11–26.

[13] E. González, P. Maimí, P. Camanho, C. Lopes, N. Blanco, Effects of ply clustering in laminated composite plates under low-velocity impact loading, Composites Science and Technology 71 (6) (2011) 805–817.

[14] E. Abisset, F. Daghia, X. Sun, M. R. Wisnom, S. R. Hallett, Interaction of inter-and intralaminar damage in scaled quasi-static indentation tests: Part 1– experiments, Composite Structures 136 (2016) 712–726.

[15] D. Bull, S. Spearing, I. Sinclair, Investigation of the response to low velocity impact and quasi-static indentation loading of particle-toughened carbon-fibre composite materials, Composites Part A: Applied Science and Manufacturing 74 (2015) 38–46.

[16] MATLAB, version 8.5.0 (R2015a), The MathWorks Inc., Natick, Massachusetts, 2015.

[17] R. M. Jones, Mechanics of composite materials, CRC Press, 1998.

[18] J. M. Whitney, Structural analysis of laminated anisotropic plates, CRC Press, 1987.

[19] D. Liu, Impact-induced delaminationa view of bending stiffness mismatching, Journal of Composite Materials 22 (7) (1988) 674–692.

[20] S. García-Rodríguez, J. Costa, V. Singery, I. Boada, J. Mayugo, The effect interleaving has on thin-ply non-crimp fabric laminate impact response: X-ray tomography investigation, Composites Part A: Applied Science and Manufacturing 107 (2018) 409–420.

[21] ASTM D7136/D7136M-15, Standard test method for measuring the damage resistance of a fiber reinforced polymer matrix composite to a drop weight impact event, 2015.

[22] Y. Liv, A contribution to the understanding of compression after impact of composite laminates, PhD thesis, University of Girona; 2017.

[23] P. Maimí, P. P. Camanho, J. Mayugo, C. Dávila, A continuum damage model for composite laminates: Part I–Constitutive model, Mechanics of Materials 39 (10) (2007) 897–908.

[24] P. Maimí, P. P. Camanho, J. Mayugo, C. Dávila, A continuum damage model

for composite laminates: Part II–Computational implementation and validation, Mechanics of Materials 39 (10) (2007) 909–919.

[25] P. P. Camanho, C. G. Dávila, S. T. Pinho, L. Iannucci, P. Robinson, Prediction of in situ strengths and matrix cracking in composites under transverse tension and in-plane shear, Composites Part A: Applied Science and Manufacturing 37 (2) (2006) 165–176.

[26] P. P. Camanho, S. R. Hallett, Numerical modelling of failure in advanced composite materials, Woodhead Publishing, 2015.

[27] E. González, P. Maimí, E. Martín-Santos, A. Soto, P. Cruz, F. M. de la Escalera, J. S. de Aja, Simulating drop-weight impact and compression after impact tests on composite laminates using conventional shell finite elements, International Journal of Solids and Structures 144 (2018) 230–247.

[28] Abaqus, Inc, Abaqus version 6.12 user manual, Simulia, Providence, RI, USA.

[29] M. Benzeggagh, M. Kenane, Measurement of mixed-mode delamination fracture toughness of unidirectional glass/epoxy composites with mixed-mode bending apparatus, Composites Science and Technology 56 (4) (1996) 439–449.

[30] W. Tan, B. G. Falzon, L. N. Chiu, M. Price, Predicting low velocity impact damage and compression-after-impact (CAI) behaviour of composite laminates, Composites Part A: Applied Science and Manufacturing 71 (2015) 212–226.

[31] A. Soto, E. González, P. Maimí, F. M. de la Escalera, J. S. de Aja, E. Alvarez, Low velocity impact and compression after impact simulation of thin ply laminates, Composites Part A: Applied Science and Manufacturing 109 (2018) 413–427.

[32] A. Soto, E. González, P. Maimí, J. Mayugo, P. Pasquali, P. Camanho, A methodology to simulate low velocity impact and compression after impact in large composite stiffened panels, Composite Structures 204 (2018) 223–238.

[33] P. P. Camanho, P. Maimí, C. Dávila, Prediction of size effects in notched laminates using continuum damage mechanics, Composites Science and Technology 67 (13) (2007) 2715–2727.

[34] D. Bull, S. Spearing, I. Sinclair, Observations of damage development from compression-after-impact experiments using ex situ micro-focus computed tomography, Composites Science and Technology 97 (2014) 106–114.

[35] J. Zhang, X. Zhang, An efficient approach for predicting low-velocity impact force and damage in composite laminates, Composite Structures 130 (2015) 85–94.

[36] G. Catalanotti, C. Furtado, T. Scalici, G. Pitarresi, F. Van Der Meer, P. Camanho, The effect of through-thickness compressive stress on mode II interlaminar fracture toughness, Composite Structures 182 (2017) 153–163.

[37] X. Xu, M. R. Wisnom, X. Sun, S. R. Hallett, Experimental determination of through-thickness compression (TTC) enhancement factor for mode II fracture energy, Composites Science and Technology.

[38] A. Quintanas-Corominas, P. Maimí, E. Casoni, A. Turon, J. A. Mayugo, G. Guillamet, M. Vázquez, A 3d transversally isotropic constitutive model for advanced composites implemented in a high performance computing code, European Journal of Mechanics-A/Solids 71 (2018) 278–291.

[39] C. Lopes, S. Sádaba, C. González, J. Llorca, P. Camanho, Physically-sound simulation of low-velocity impact on fiber reinforced laminates, International Journal of Impact Engineering 92 (2016) 3–17.

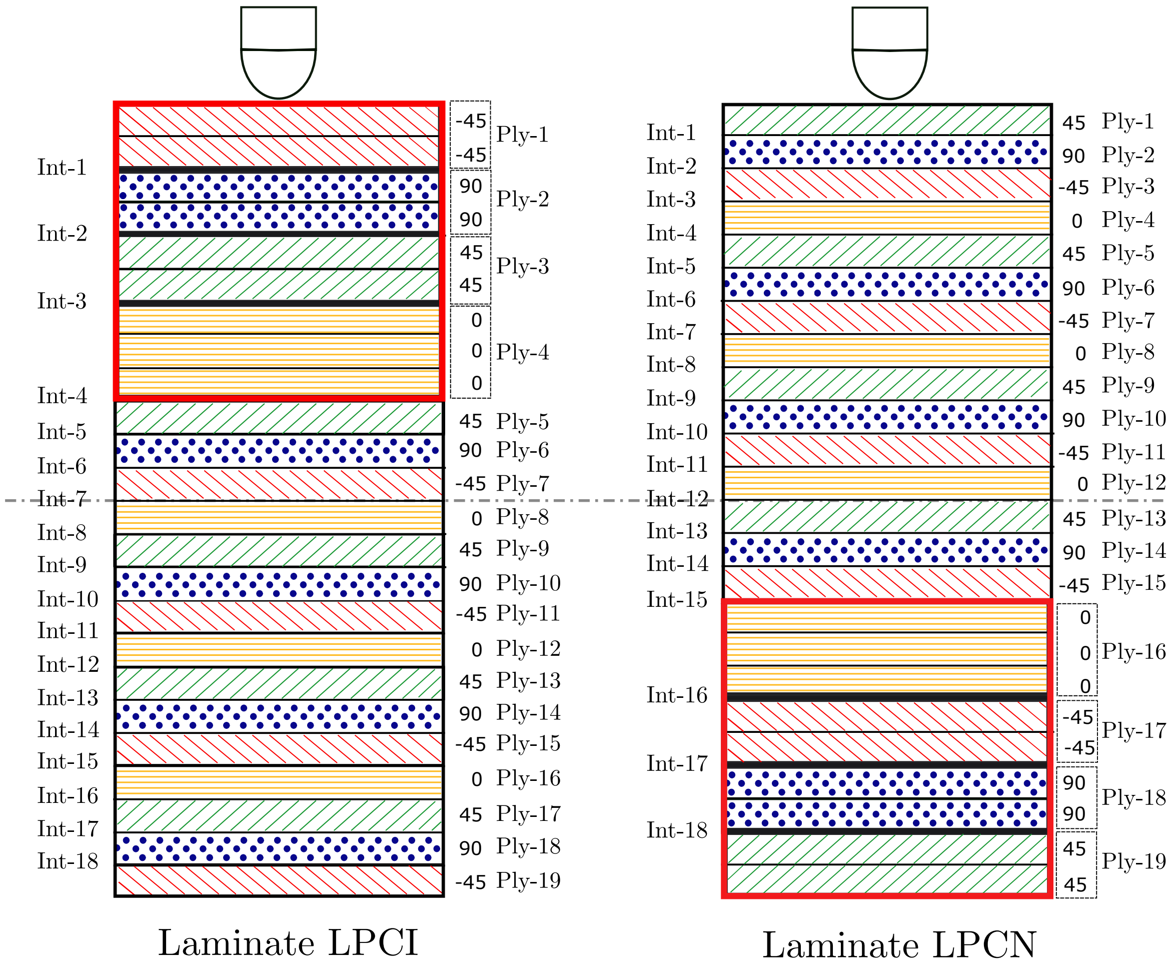

Figure 1: Unsymmetrical laminate LPCI with ply clustering at the impacted side (left) and laminate LPCN with ply clustering at the non-impacted side (right), which is produced by flipping the laminate LPCI upside down. Flipping upside down only interchanges the 45s by -45s plies, i.e., it does not alter the in-plane and bending stiffness in the 0° and 90° directions.

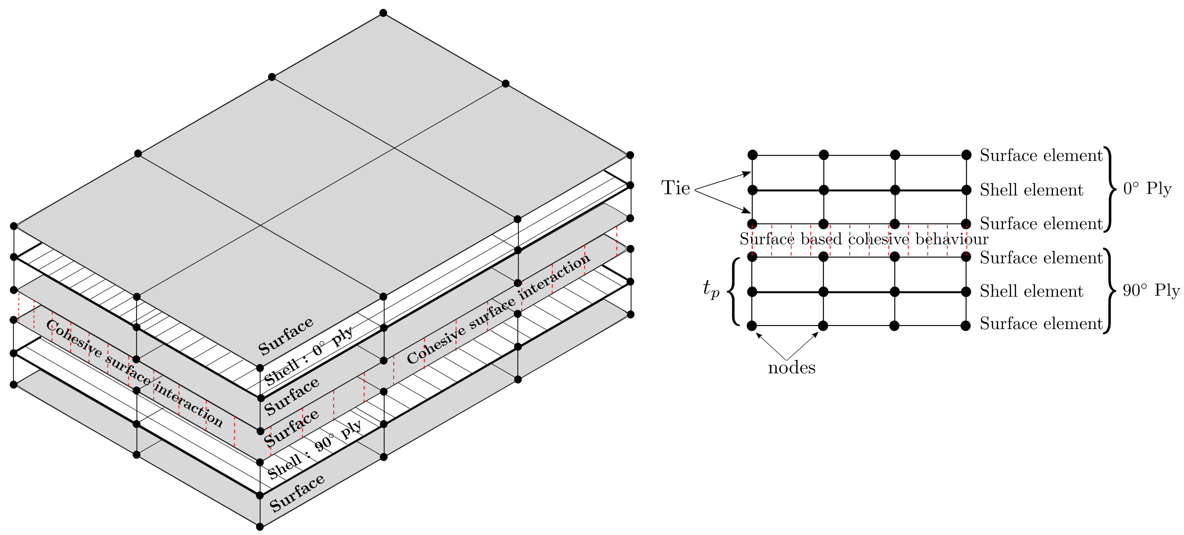

Figure 2: Schematic representation of the modelling strategy, where each ply is modelled using a shell element sandwiched between two surface elements using a tie interaction. Surface based cohesive interaction is assigned between the bottom surface of the top ply and the top surface of the bottom ply. t_p marks the thickness of the modelled ply, and there is no thickness defined between the surface elements.

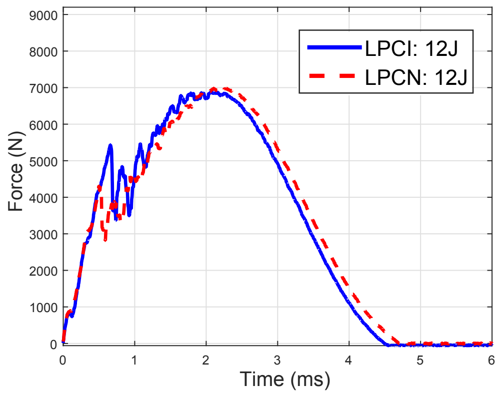

(a)

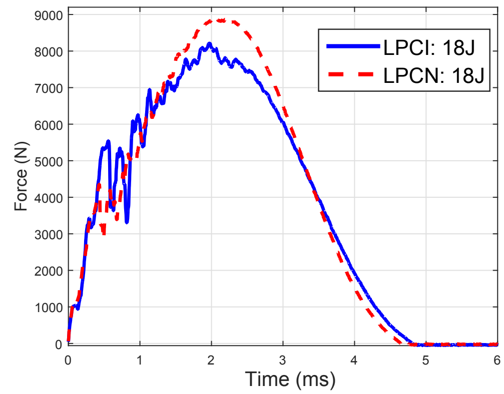

(b)

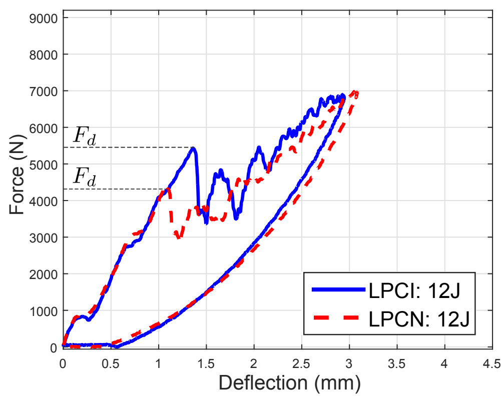

(c)

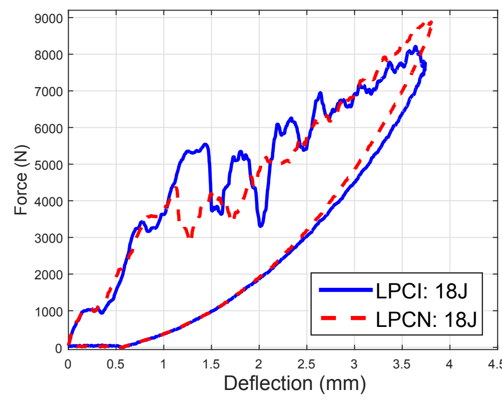

(d)

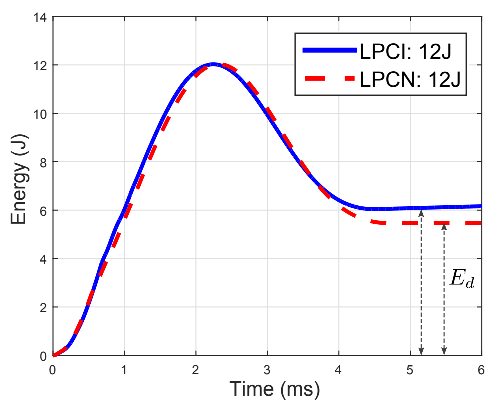

(e)

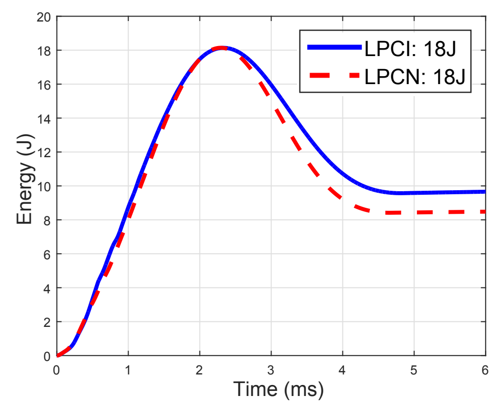

(f)

Figure 3: Force-time ((a),(b)), force-deflection ((c),(d)), and energy-time ((e),(f)) response curves for LPCI and LPCN for 12 J and 18 J impact energies.

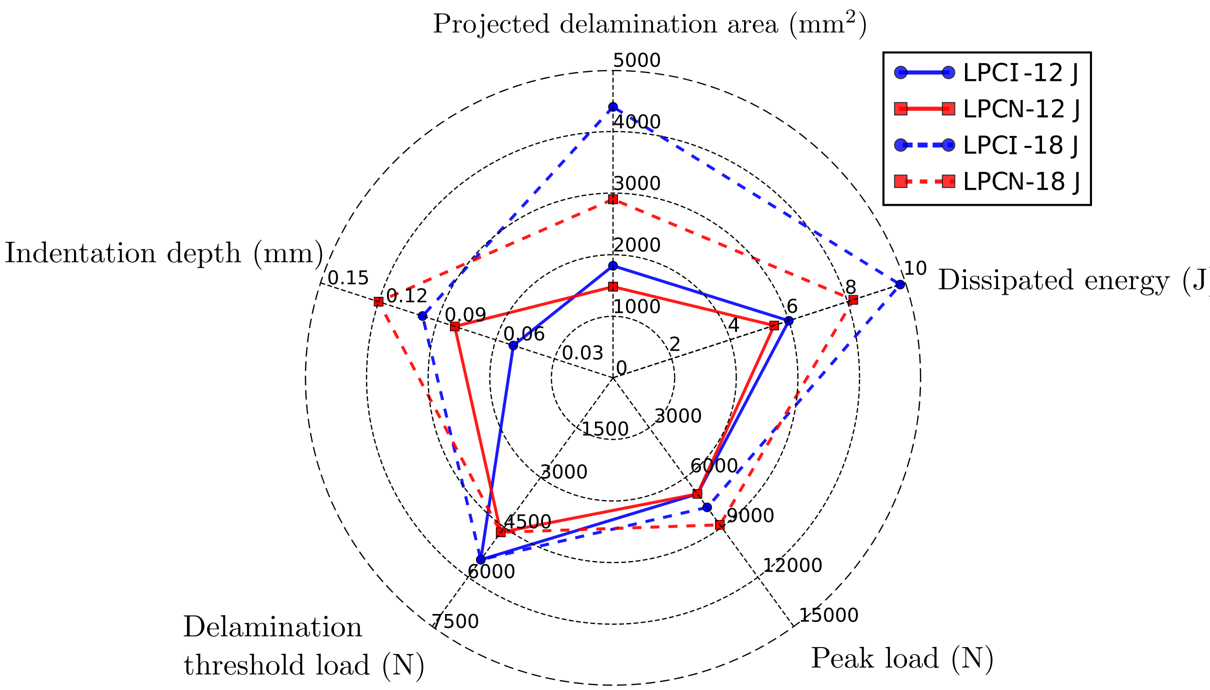

Figure 4: Quantitative overview of impact damage resistance parameters of LPCI and LPCN at both impact energies.

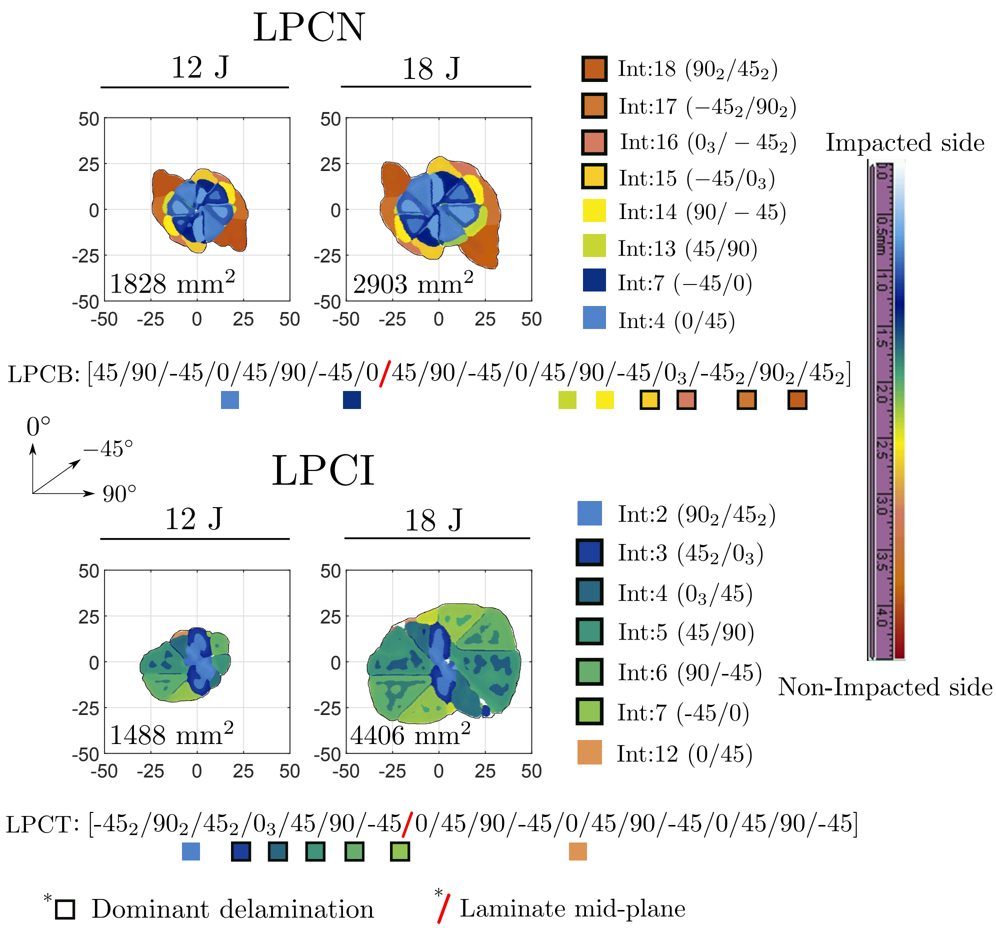

Figure 5: C-scan images of LPCN and LPCI inspected from the impacted face for 12 J and 18 J impact energies. Projected delamination area, identified delaminated interfaces and dominant delaminations are marked (The colour bar helps to identify the location of delamination in the thickness direction, and the axes are provided in millimetres).

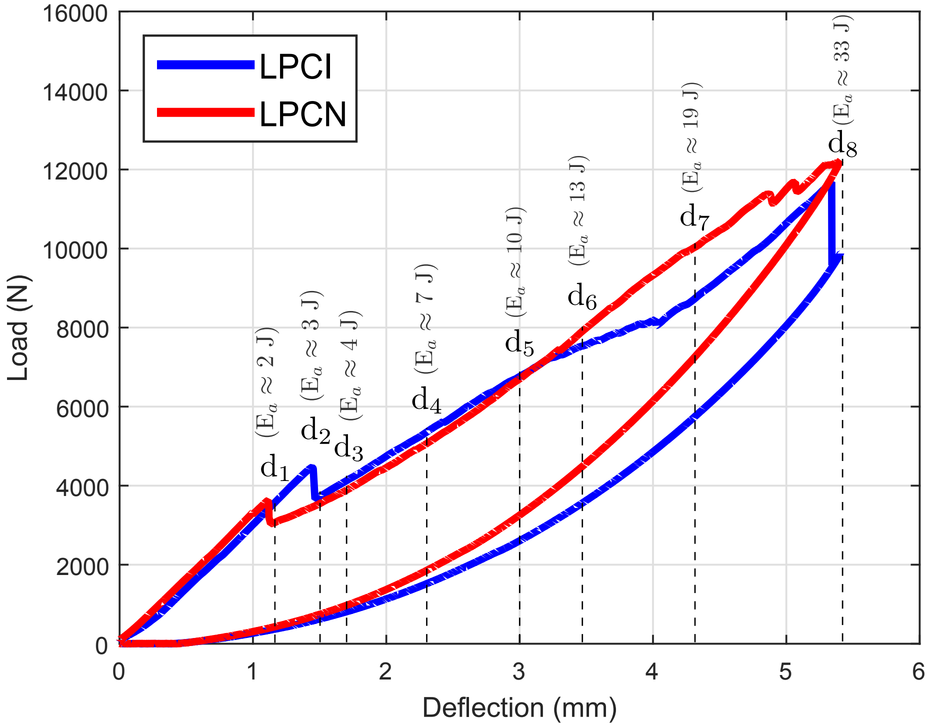

Figure 6: Load-deflection curve for the maximum indenter displacement $d_8 = 5.4$ mm for LPCN and LPCI, also showing the various other indenter displacements used in the study (The respective energy applied, E_a, is also marked for each indenter displacement).

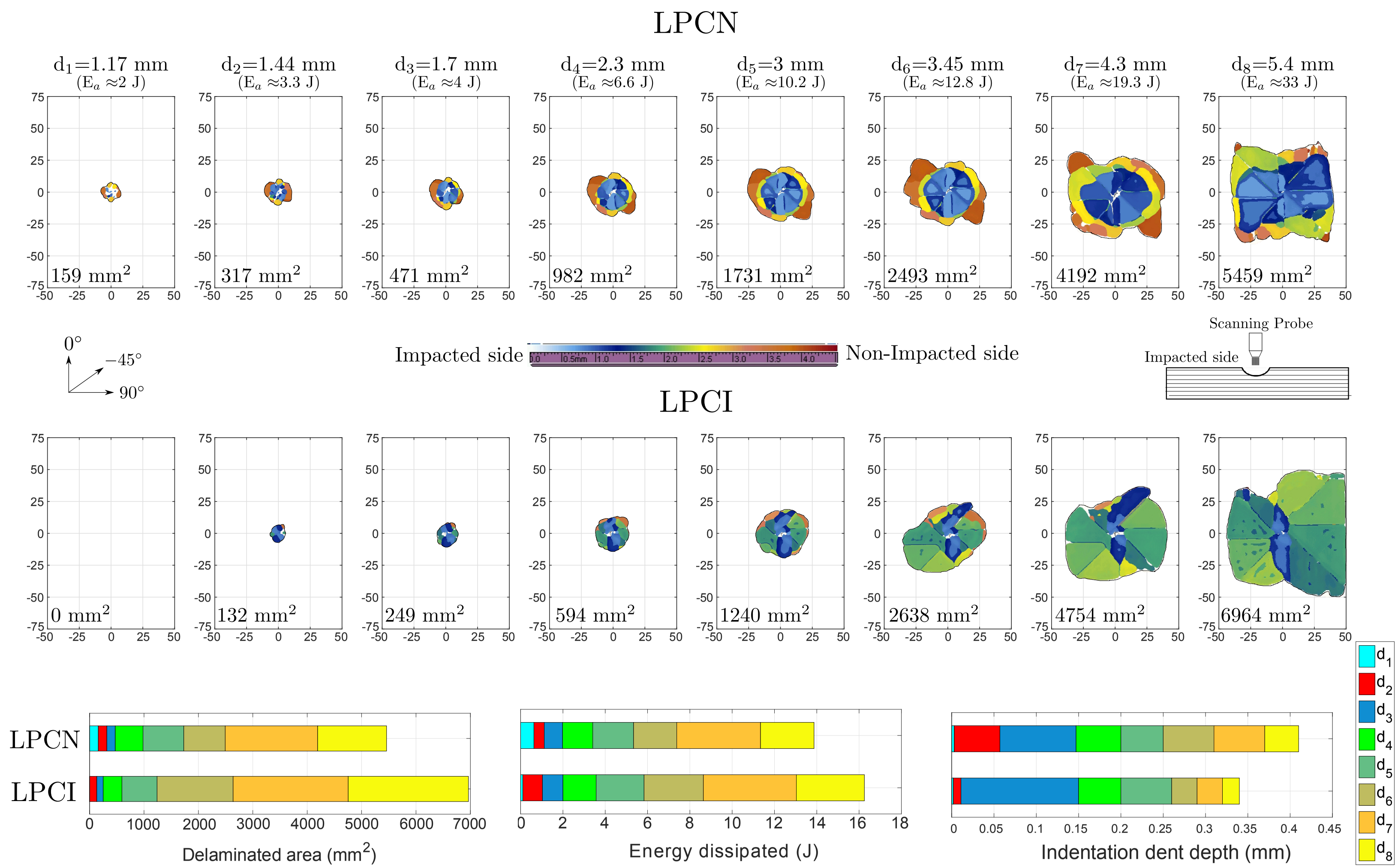

Figure 7: (a) Impacted face C-scan images revealing the delamination initiation and propagation for various indenter displacements (b) Quantitative evolution of damage resistance parameters for all indenter displacements for LPCN and LPCI.

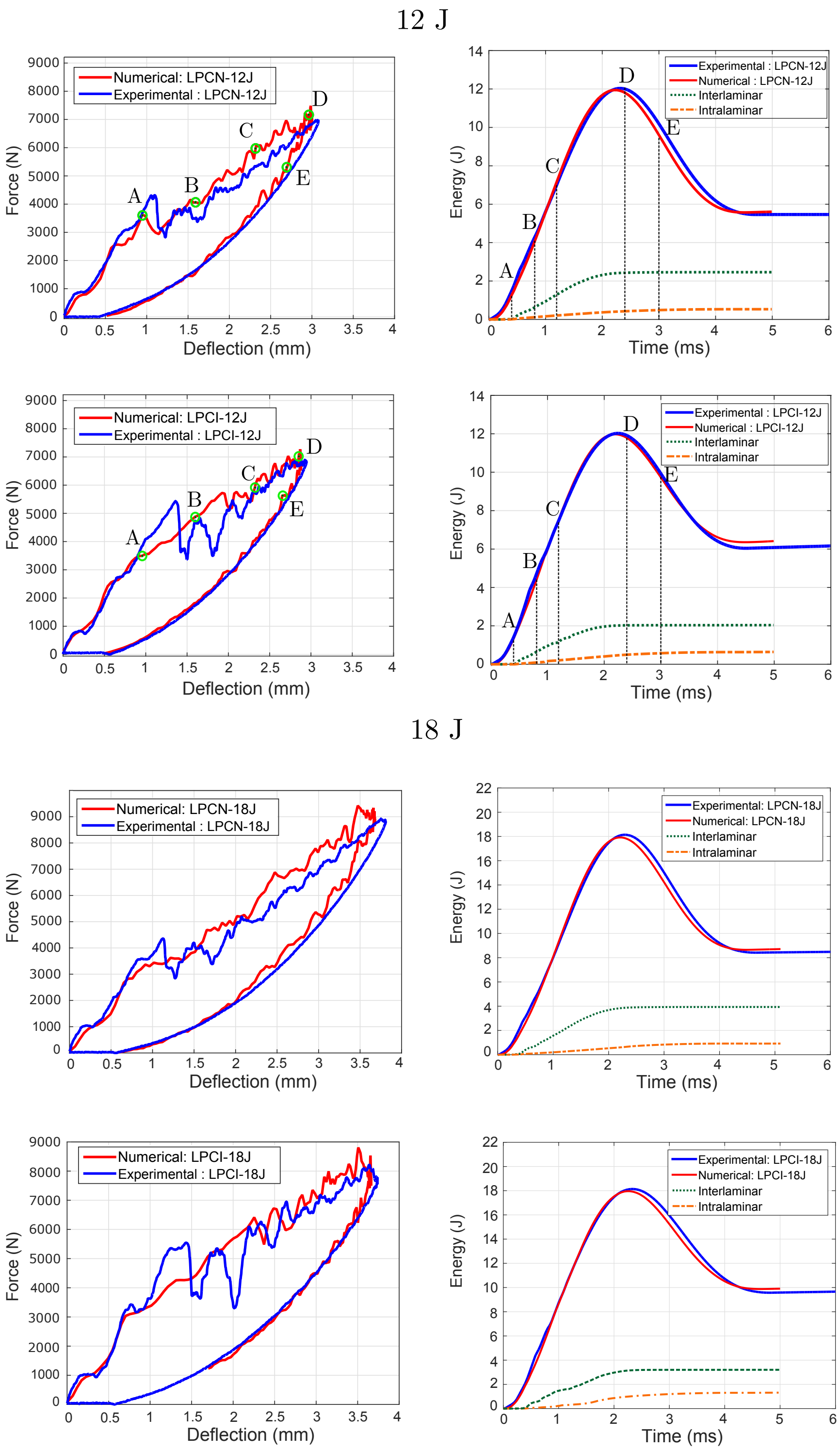

Figure 8: Numerical prediction of the impact response of LPCN and LPCI laminates compared with the experimental data for both 12 J and 18 J. Selected displacements (A to E) for energy dissipation study (in Fig. 10) are also marked for the 12 J energy case.

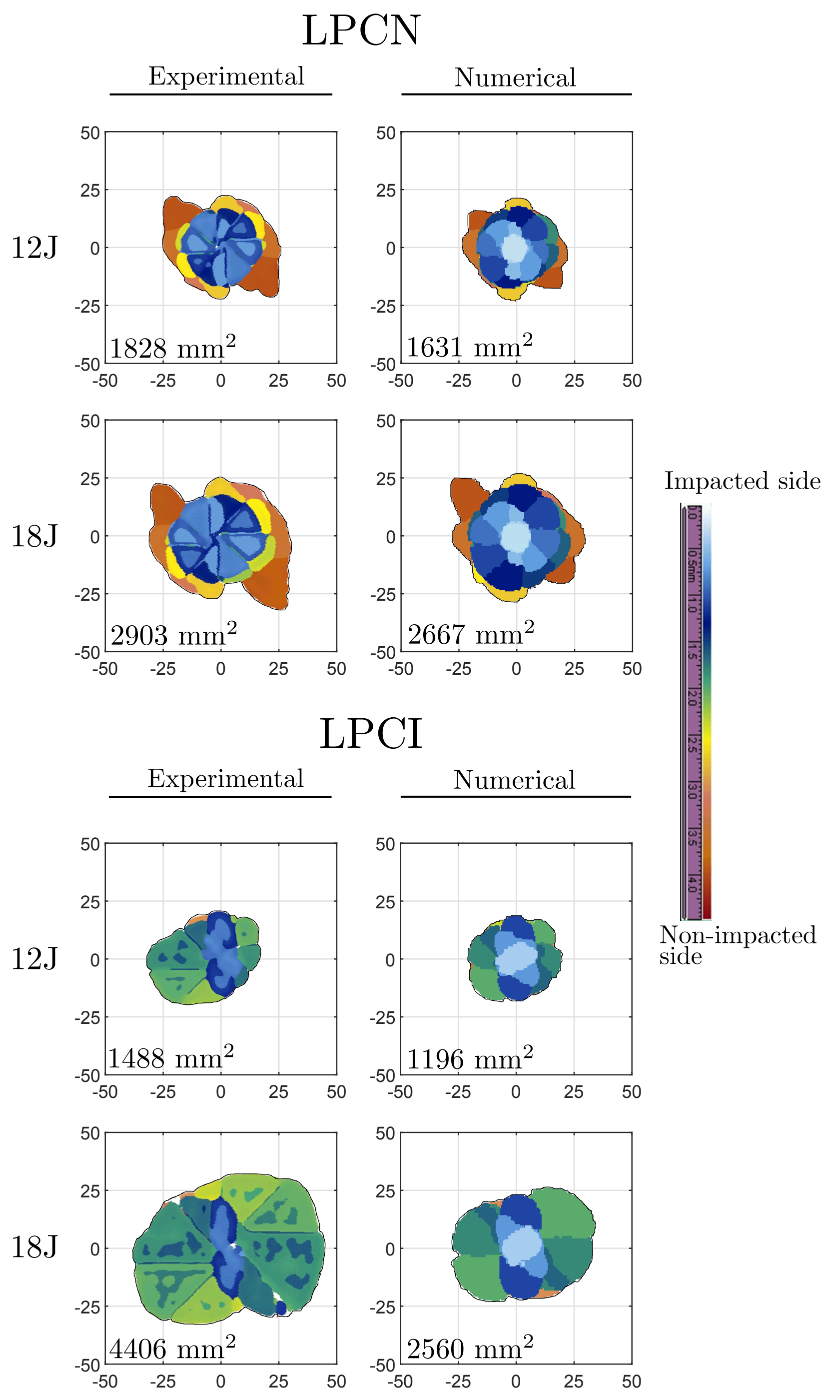

Figure 9: Comparison of the virtual C-scan from numerical study with the C-scan after impact testing for LPCN and LPCI for both 12 J and 18 J. Projected delamination area is provided in the bottom left corner of each box.

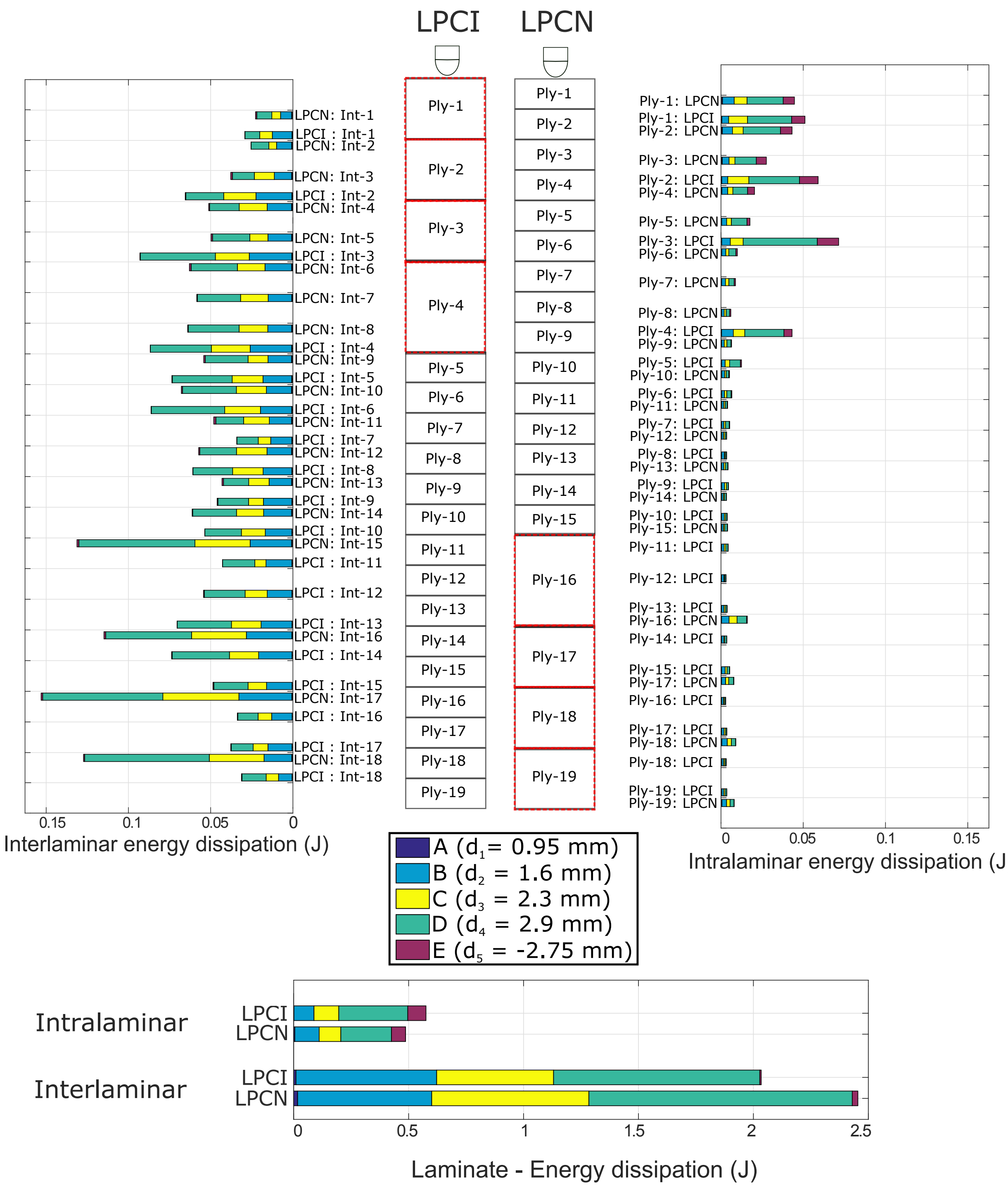

Figure 10: Illustration of the laminates and their plies along with the amount of inter and intralaminar energy dissipated for each ply and interface of both the laminates. Note that the clustered plies are considered as a single ply and hence, for example, interface 1 of LPCI is compared with the interface 2 of LPCN. The different colour codes represent the energy dissipated with the different displacement steps (A to E, as shown in Fig. 8). The total dissipated energies (inter- and intralaminar) by the laminates are also compared at the bottom.